

Detecting gravitational waves sources – BHs, NSs, BHNS – with LISA

Nazeela Aimen, Syed Ali Mohsin Bukhari, Asad Ali

Department of Applied Mathematics and Statistics, Institute of Space Technology, Islamabad 44000, Pakistan.

Space and Astrophysics Research Lab (SARL), Institute of Space Technology, Islamabad 44000, Pakistan.

Abstract—The double compact objects (DCOs) present a broad range of possible GW detections in our MW galaxy. Here we present a case study on the detection of DCOs with progenitors having high metallic content. Furthermore, the effects of eccentricity on the ZAMS stage on the evolution of binaries is also checked via a comparative analysis for two identical data sets. The binaries were generated using the Compact Object Mergers: Population Astrophysics and Statistics (COMPAS) suite, followed by their distribution in a metallicity–age dependent Milky Way galaxy model.

For a 4-year LISA mission, this study predicts a detection rate between 83-124(86-131) detections for data sets with variable ZAMS and zero ZAMS eccentricity respectively. Out of these, 21-45(17-36) are BHs, 17-44(17-38) are NSs, 6-28(11-29) are BHNSs and 13-39(21-46) are NSBHs. NSBH were considered separate from BHNS as the stellar evolution indicates that the primary star in the binary ended up as a NS instead of a BH. It was also observed that some common binaries end up in different DCO stages in both data sets.

Index Terms—Gravitational waves, gravitational wave detectors, black holes, neutron stars, double compact objects

I. INTRODUCTION

The gravitational waves (GW) were predicted a year after the final formulation of the general theory of relativity (GR) by Albert Einstein [18]. Similar to electromagnetic waves, the GWs travel at the speed of light [1, 17]. However, unlike electromagnetic waves, the GW stretches and squeezes the space itself thus causing spatial disturbances. The detection of Hulse-Taylor binary [25], and the subsequent observation of a seven years time span [49] stirred a great interest in the GW observations. It wasn't until 2015 that the first direct observation of GW was made by LIGO and VIRGO collaborations [1]. The lower frequency bound for both the aLIGO and VIRGO detectors is around 10 Hz [2, 15].

The Laser Interferometer Space Antenna (LISA) has three spacecrafts that form a triangle, each side 2.5 million km long [39, 43]. Operating in the frequency range of $1 \times 10^{-5} \text{ Hz} \leq f \leq 1 \times 10^{-1} \text{ Hz}$ LISA will be able to observe the sources millions of years before they merge. The early detection capability will help better constrain and determine the orbital parameters of the observed binaries. Some sources detectable by LISA are the extreme mass ratio inspirals (EMRIs) [14, 23, 29] and galactic binaries [1, 16, 52]. This makes LISA also capable of mapping Milky Way galaxy's structure. Another interesting class detectable by LISA is the double white dwarf stars (DWDs) which are reported to be

abundant in our MW galaxy and have a substantial detection in LISA as well [30, 35, 44, 54].

A lot of effort has been put into the detection of potential GW sources for LISA, the resolution of issues that might be associated with the background data, and proposals of new candidates as GW sources for LISA [see, for example, 3, 4, 5, 8, 9, 13, 22, 24, 28, 32, 35, 40, 44, 46, 47, 52, 55]. The detections of these sources will provide us with a better understanding of not only the evolution phases but also the endpoints of stellar evolution.

The goals of this research are,

- 1) to predict the number of DCO binaries that can be detected via LISA in our Milky Way galaxy,
 - a) to determine whether extra galactic sources are LISA detectable,
- 2) to make a general detection comparison between DCO binaries with and without an initial eccentricity.

This research paper is structured as follows, in section II we discuss the generation of binary systems using COMPAS suite. In section III we give a general overview of the methodology adopted in this research for evolving the stars from ZAMS to DCOs, from DCOs to merger stage, and their detection by LISA as well. The evolution of binaries and their detection is discussed in section IV.

II. POPULATION SYNTHESIS

The population synthesis for the detections of the double compact objects (DCOs) was performed using the Compact Object Mergers: Population Astrophysics and Statistics (COMPAS; [42, 48, 50]) suite. COMPAS is a rapid stellar evolution suite and can evolve both single and binary stars following the details outlined by [26, 27]. A list of selected papers that make use of the COMPAS suite is also available on the COMPAS website.¹

This study makes use exclusively of the binary star evolution (BSE) synthesis method. The default parameters used by the COMPAS software are listed in table 1 in the COMPAS paper [42].

Except for supernova mass remnant prescription, initial eccentricity (e_i), metallicity (z), and pulsar evolution, all other parameters were taken at the default value. For a one-to-one correspondence between the two generated data sets, the seed numbers were kept constant.

¹<https://compas.science/science.html>

For the mass of primary star, we draw the values from Kroupa initial mass function (IMF) with $m_1 \in [5, 150] M_{\odot}$ [31]. For the secondary star, we randomly draw from uniform distribution to satisfy $q \equiv m_2/m_1$, where $q \in [0, 1]$ [45]. An additional constraint of $m_2 \geq 0.1 m_1$ was placed on m_2 as this is the minimum mass necessary for a star to be considered as a main sequence star.

For the semi-major axis of the binary, we drew the parameter values from a flat-in-the-log distribution with $a_i \in [0.1, 1000]$ AU, such that $p(a_i) \propto 1/a_i$ [36].

For the remnant mass prescription, we first considered the Fryer delayed model [21]. However, this resulted in a concentration of NS mass around $\sim 1.28 M_{\odot}$. To avoid this concentration of NS final mass, we used Müller & Mandel prescription (M&M) [33]. M&M is a stochastic remnant mass model that offers a smoother mass distribution for NS. We also switched the **evolve_pulsar** flag to **True** during population synthesis.

For metallicity, we drew the values from a Beta(5, 80) distribution. The main motivation behind the selection of such biased distribution is the higher metallic content of present-day stars. The population III stars were primarily composed of pure hydrogen and their deaths produced heavier metals in the Universe. By this extension, the stars that are present now or those that will merge now must have higher metallic content. As such, we also speculate that having stars with higher metallic content might produce more NSNS or NS-BH pairs for detection rather than BH-BH pairs.

For eccentricity, we make use of two cases,

- Case I: All the binary systems are generated using a uniform distribution, $e \in (0, 1]$.
- Case II: All the binary systems are generated with circular orbits, i.e., $e = 0$.

From here on the data set for Case I and Case II will be represented by Θ_1 and Θ_2 respectively. Details about the selection of metallicity and eccentricity values in COMPAS are provided in appendix A.

III. EVOLUTION METHODOLOGY

We first generated 1×10^7 values for metallicity using the beta distribution within the COMPAS limits. We denote the zero-age main sequence (ZAMS) parameters of the binaries as,

$$m_{1\text{ZAMS}}, m_{2\text{ZAMS}}, a_{\text{ZAMS}}, e_{\text{ZAMS}}, Z, \phi \quad (1)$$

COMPAS evolves the binaries up to 13.7 Gyr. We represent the resulting double compact object (DCO) parameters as,

$$m_{1\text{DCO}}, m_{2\text{DCO}}, a_{\text{DCO}}, e_{\text{DCO}}, t_{\text{evolve}}, Z, \phi, \quad (2)$$

where Z is the metallicity of the binary system, ϕ is the seed number, t_{evolve} is the time required to form DCO from ZAMS. a_{ZAMS} , a_{DCO} , e_{ZAMS} , and e_{DCO} are the semi-major axis and eccentricity of the binary orbit at ZAMS and DCO formation respectively. Once the DCOs have been formed, we move out of the COMPAS suite. For the LISA detection, the DCO formed from the set of binaries were checked for an evolutionary stop, i.e., only those binaries were selected that

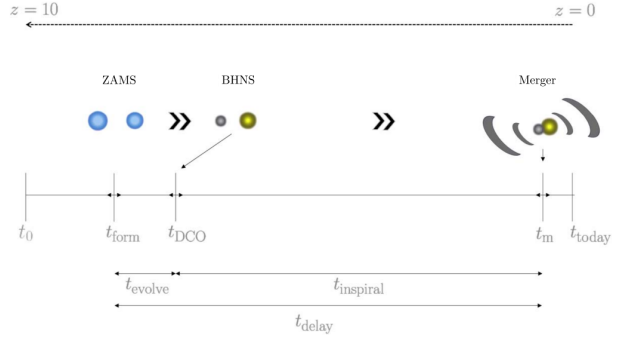


Fig. 1: Schematic diagram showing various time intervals for a binary system from ZAMS formation, to DCO, and merger. The figure is taken from [42].

will merge within the Hubble time. The selected candidates were then provided to the python framework LEGWORK [51] that evolved them from the DCO stage to the merger state. It evolved the binaries using equations from [37, 38].

The DCO–merger evolution method follows the one outlined by [52] closely. The evolution was done such that the MW galaxy instance was divided into bins based on the metallicity values of the evolving binaries. The evolution time was calculated after taking into consideration the ZAMS-DCO evolution time and the lookback time of all the MW points within the metallicity bins. If a binary, at DCO stage, had a resultant merger time greater than the difference of its lookback time and ZAMS-DCO evolution time, it was marked as an inspiralling binary. Each inspiralling binary was then evolved at every point within the corresponding metallicity bin using LEGWORK to a million year before its merger time. At this stage, the resulting LISA parameters of interest were,

$$a_{\text{LISA}}, e_{\text{LISA}}, f_{\text{LISA}} \quad (3)$$

The SNR was then calculated by further evolving them for the LISA mission duration of four years. The detection is made based on the signal-to-noise ratio (SNR) of the binary averaged over sky position, polarization, and orientation using the following expression from [19],

$$\rho^2 = \sum_{n=1}^{\infty} \int_{f_{n,i}}^{f_{n,f}} \frac{h_{c,n}^2}{f_n^2 S_n(f_n)} df_n, \quad (4)$$

where n is the GW harmonic, f_n represents the orbital frequency of n^{th} harmonic. The parameter $S_n(f_n)$ is the LISA sensitivity curve function [43], and $h_{c,n}$ is the characteristic strain of the n^{th} GW harmonic [6].

$$h_{c,n}^2 = \frac{2^{5/3}}{3\pi^{4/3}} \frac{(GM_c)^{5/3}}{c^3 D_L^2} \frac{1}{f_{\text{orb}}^{1/3}} \frac{g(n, e)}{n F(e)} \quad (5)$$

IV. EVOLUTION AND DETECTION

After running the simulations as outlined in section II, we obtained 12254 DCOs ($\sim 0.12254\%$). Following section III, we obtain the required parameter values of only 6539 DCOs that merged within Hubble time ($\sim 53.3621\%$) thus making

them a potential LISA source.² The Hubble time merge rate of DCOs is given in table I,

| Type | BHBH | NSNS | BHNS | | | |
|-------|-----------|-------------|-----------|------------|--|--|
| | | | NSBH | | | |
| | | | BHNS | | | |
| M / T | 492 / 663 | 4752 / 9219 | 480 / 868 | 815 / 1504 | | |
| D / M | 348 / 492 | 1281 / 4752 | 300 / 480 | 327 / 815 | | |

TABLE I: **RowI** shows the merging (M) vs total (T) formed DCOs in this study, **RowII** shows the uniquely detectable (D) vs the merging (M) DCOs from this study for Θ_1 .

The highest merging rate in this study is of BHBH pairs ($\sim 74.21\%$), followed by NSBH pairs ($\sim 55.30\%$), BHNS ($\sim 54.19\%$) and lastly NSNS DCO type ($\sim 51.55\%$) comprising the ‘candidate binaries’, see table I **RowI**.³

Using the LEGWORK framework [51], these binaries were than checked for their inspiral phase using the t_{evolve} ⁴ and t_{lookback} ⁵. The difference between lookback and evolution time of a binary was required to be less than its merger time⁶. Out of the merging binaries, BHBH pairs had the most detectable sources in the data set, ($\sim 70.73\%$), followed by NSBH pair ($\sim 62.5\%$), BHNS pair ($\sim 40.12\%$) and lastly NSNS pair ($\sim 26.96\%$), see table I **RowII**.

As the number of detectable binaries in our study was small compared to the total generated population,⁷ multiple detections of a single binary object are present in the final output. Table II shows selective details about mass of progenitor and their evolutionary ends for maximum and minimum mass at ZAMS and DCO stages. In appendix C we present the number of detection and mean values for selected parameters⁸ across the hundred instances of MW galaxies. The number of detections across all the MW instances came out to be 12841.

The predicted distribution of the LISA detectable sources are plotted over its expected sensitivity curve [43], in figure 2. The x-axis shows the dominant frequency, the frequency accumulating the largest SNR, for the eccentric binaries. Furthermore, on y-axis we plot the amplitude spectral density (ASD), including the contribution from all harmonics. The gap between the detected binaries and the LISA curve in the graph is the SNR criteria, ($\text{SNR} > 7$). The size of the points varies with metallicity; high metallic sources have larger shapes and vice versa. The color scheme is based on the eccentricity of detected binaries with a reverse red-yellow-green color palette⁹, going from green, yellow and finally red in increasing order of eccentricity values.

Majority of the binary population reside on the lower end of LISA spectrum. For **Row1**, the peak orbital frequency occurs

²Overall, only $\sim 0.06539\%$ binary system formed into DCOs that merge within Hubble time.

³Such DCO pairs which can have a potential LISA detection.

⁴Obtained via COMPAS.

⁵Obtained via galaxy synthesis.

⁶Obtained via LEGWORK framework.

⁷Due to not using any technique that forces DCO production, e.g., STROOPWAFEL [12].

⁸The selected parameters include, $m_{1\text{DCO}}$, $m_{2\text{DCO}}$, a_{DCO} , e_{DCO} , Z , t_{evol} , t_{lookback} , and SNR.

⁹https://matplotlib.org/stable/gallery/color/colormap_reference.html

| Parameters | MAX | ZAMS details | | DCO details | | MIN | ZAMS details | | DCO details | |
|----------------------------------|---------|--------------|-----------|-------------|-----------|--------|--------------|-----------|-------------|-----------|
| | | Primary | Secondary | Primary | Secondary | | Primary | Secondary | Primary | Secondary |
| Binary Black Holes | | | | | | | | | | |
| $m_{1\text{ZAMS}}$ | 149.836 | 149.836 | 115.624 | 10.386 | 10.395 | 13.007 | 13.007 | 12.500 | 2.216 | 2.601 |
| $m_{2\text{ZAMS}}$ | 131.178 | 148.802 | 131.178 | 8.662 | 8.459 | 12.500 | 13.007 | 12.500 | 2.216 | 2.601 |
| $m_{1\text{DCO}}$ | 43.308 | 57.334 | 57.334 | 43.308 | 43.308 | 2.022 | 26.497 | 26.493 | 2.022 | 7.104 |
| $m_{2\text{DCO}}$ | 43.308 | 57.334 | 57.334 | 43.308 | 43.308 | 2.018 | 42.088 | 30.574 | 7.456 | 2.018 |
| Binary Neutron Stars | | | | | | | | | | |
| $m_{1\text{ZAMS}}$ | 54.41 | 54.41 | 13.76 | 1.614 | 1.235 | 8.546 | 8.546 | 7.822 | 1.26 | 1.193 |
| $m_{2\text{ZAMS}}$ | 25.571 | 25.586 | 25.571 | 1.480 | 1.693 | 6.626 | 13.01 | 6.626 | 1.26 | 1.194 |
| $m_{1\text{DCO}}$ | 1.938 | 14.022 | 13.938 | 1.938 | 1.487 | 1.135 | 10.319 | 10.019 | 1.135 | 1.392 |
| $m_{2\text{DCO}}$ | 1.991 | 13.919 | 13.574 | 1.681 | 1.991 | 1.132 | 11.674 | 11.021 | 1.518 | 1.132 |
| Neutron Star – Black Hole | | | | | | | | | | |
| $m_{1\text{ZAMS}}$ | 53.708 | 53.708 | 29.613 | 1.439 | 15.342 | 8.971 | 8.971 | 8.847 | 1.260 | 3.869 |
| $m_{2\text{ZAMS}}$ | 42.242 | 42.289 | 42.242 | 1.598 | 7.382 | 8.665 | 9.164 | 8.665 | 1.260 | 2.062 |
| $m_{1\text{DCO}}$ | 1.935 | 14.090 | 13.959 | 1.935 | 3.822 | 1.137 | 27.186 | 17.676 | 1.137 | 9.646 |
| $m_{2\text{DCO}}$ | 15.342 | 53.708 | 29.613 | 1.439 | 15.342 | 2.003 | 12.472 | 12.033 | 1.608 | 2.003 |
| Black Hole – Neutron Star | | | | | | | | | | |
| $m_{1\text{ZAMS}}$ | 145.467 | 145.467 | 46.439 | 9.907 | 1.593 | 11.626 | 11.626 | 11.608 | 2.216 | 1.522 |
| $m_{2\text{ZAMS}}$ | 108.489 | 140.091 | 108.489 | 12.217 | 1.415 | 10.072 | 23.144 | 10.072 | 2.922 | 1.206 |
| $m_{1\text{DCO}}$ | 15.106 | 90.844 | 76.11 | 15.106 | 1.669 | 2.004 | 13.125 | 12.872 | 2.004 | 1.785 |
| $m_{2\text{DCO}}$ | 1.945 | 29.142 | 15.445 | 4.341 | 1.945 | 1.141 | 28.317 | 22.834 | 5.61 | 1.141 |

TABLE II: Maximum and minimum values for masses of both ZAMS and DCO type stars in the BHBH data set with their respective counterparts. The ‘MAX’ and ‘MIN’ columns represent the maximum and minimum value for the given parameter respectively. The ‘ZAMS details’ and ‘DCO details’ column list the value of primary and secondary components of the binary and respective stage of evolution with ‘MAX’ and ‘MIN’ value of the parameter at that stage. All the masses are given in units of solar mass.

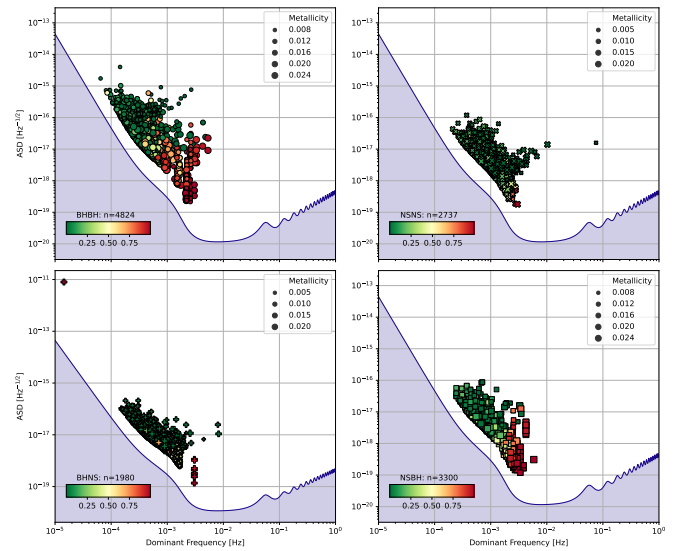


Fig. 2: Detectable sources’ characteristic strain vs. dominant frequency in our simulations are shown on the LISA sensitivity curve for Θ_1 data set. The sources are color-coded based on their eccentricities, green for low and red for high eccentric sources.

at 0.174 mHz, 0.5308 mHz, 0.3039 mHz, and 0.4016 mHz respectively for BHBH, NSNS, BHNS and NSBH population. Similarly, for **Row2**, the peak dominant frequency occurs at 0.3919 mHz, 1.057 mHz, 0.5828 mHz, and 0.8668 mHz respectively. The reason for such a trend can be explained through the eccentricities of the binaries. As seen from the figure 3 **Row3**, a large portion of our binaries is either low or mid-eccentric. The orbit of low eccentric binaries evolves differently than high eccentric binaries. After the formation of DCO, the low eccentric binaries emit GW in the second

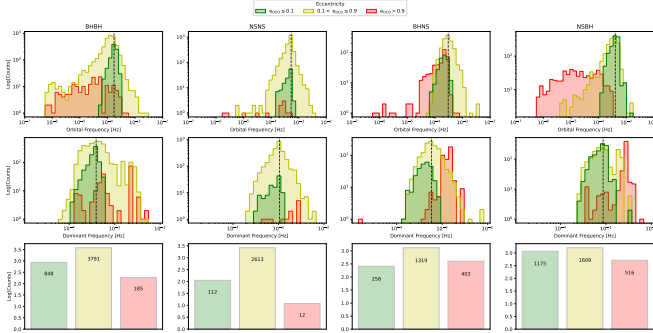


Fig. 3: **Row1:** Eccentricity characterized distribution of DCOs for their orbital frequency. **Row2:** Same as **Row1** but for the binary's dominant frequency. **Row3:** Number of binaries associated with the given eccentricity in log scale. The number inside the bars show the actual number of binaries for the given eccentricity. The log scaling was chosen due to relative lower number of DCOs in NSNS and BHNS types.

harmonic of their orbital frequency. The intensity of the frequency increases as the orbits starts to shrink. On the other hand, the DCOs with high eccentricities behave in a completely different way, i.e. their orbit decay faster, and they tend to emit GW in high harmonics [37, 38]. This also explains why even though the orbital frequency of the high eccentric binaries was small but they have larger dominant frequency.

We also notice a stray binary pair in BHNS with an $\text{ASD} \sim 8 \times 10^{-12} \text{ Hz}^{1/2}$, the highest in Θ_1 . The parameter of that particular BHNS pair are presented in table III. It is important to note that before the binary's evolution for SNR detection, it had originally evolved past its look-back time. With a lookback time of $\sim 10.393 \text{ Myr}$ and evolution time of $\sim 10.944 \text{ Myr}$, the merging time for this binary came out to be only $\sim 3.83 \text{ yr}$ when put into LEGWORK. This also explains why the parameters of this binary are identical when considering the DCO stage and near merging stage after evolving via LEGWORK. The system is emitting a dominant frequency of $\sim 1.439 \times 10^{-5} \text{ Hz}$ at a harmonic of 1, which makes it exactly the same as its orbital frequency.

| Binary Stage | m_1 [M_\odot] | m_2 [M_\odot] | a AU | e | Z | ϕ |
|--------------|---------------------|---------------------|--------|-------|-------|---------|
| ZAMS | 33.449 | 17.711 | 0.666 | 0.153 | 0.024 | 8848207 |
| DCO | 6.495 | 1.407 | 0.034 | 0.999 | // | // |

TABLE III: Parameters at difference stages of binary evolution for BHNS pair with seed number 8848207.

Figure 4 shows the percentage of different DCOs detected in the low-[α/Fe], high-[α/Fe] and bulge components of the MW instances. For low-[α/Fe] disk, the NSBH pairs have more detections than BHN pairs. Contrary to that, NSBH pairs show no detection in high-[α/Fe] disk, and fractional detection in the bulge, $\sim 0.833\%$. On the other hand, the BHNS pairs have the lowest detection rate in all three components.

BHBH is the dominant detectable pair in all three components. Except for the low-[α/Fe] component, the NSNS pair

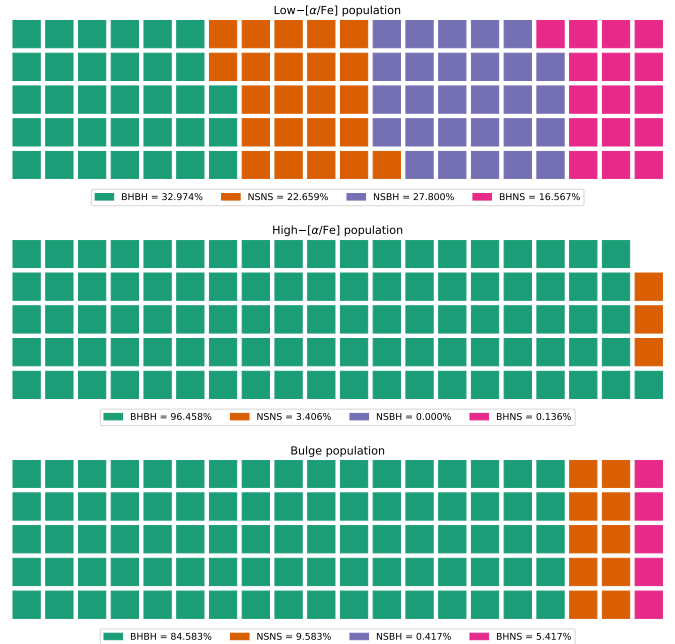


Fig. 4: Waffle charts showing percentage proportion for DCO type detections in the MW instance components in this study.

also has higher percentage of detection. For the low-[α/Fe] component we see a higher percentage of NSBH detection.

Figure 5 shows the percentage of detections in the three components regardless of the DCO type. Here we see that majority of the detections are in the low-[α/Fe] disk. This can be attributed to the biased metallicity value used in this study, Beta(5, 80). These detection percentages do align with the age-metallicity relationship as the bulge is oldest component and thus should have lower metallicity ZAMS stars. However, due to the choice of metallicity distribution, these stars were not generated in large numbers.

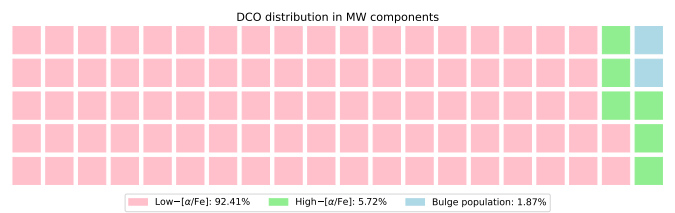


Fig. 5: Waffle chart showing the total number of detections per MW instance component in this study on the whole.

A. Maximum distance

For each DCO, there is a horizon distance i.e., the maximum distance up to which the DCO may be detectable in LISA. This is calculated using the inverse relationship between SNR (ρ) and distance [32],

$$d_{\max} = \frac{\rho(d = 1 \text{ kpc})}{\rho_{\min}} \quad (6)$$

Where ρ_{\min} is the minimum value of SNR below which the source is not detectable. We keep the detection threshold at $\rho_{\min} = 7$, and $\rho(d = 1 \text{ kpc})$ is SNR of the source if it was at 1 kpc distance from the detector. We calculated the SNR of all the detected sources at 1 kpc distance using the python package LEGWORK [51]. Afterward, their maximum distances (d_{\max}) were calculated.

Figure 6 shows the mean maximum distances for all the detected sources. The black line shows the average maximum distance for all the types combined. The LISA sensitivity curve is also overlaid on the graph.

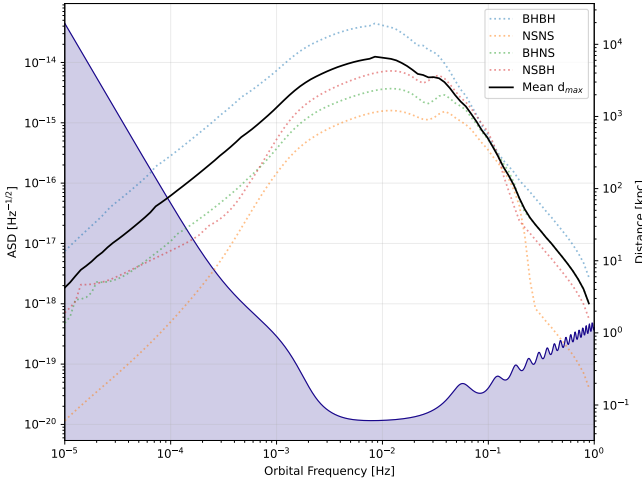


Fig. 6: Mean maximum distances for all of the different types of DCO corresponding to their orbital frequency. The overall average maximum detection distance is shown by a black line.

BHBH pairs can be observed up to an average distance of ~ 19.5 Mpc. For NSNS, BHNS, and NSBH the maximum distance came out to be ~ 1.21 Mpc, ~ 4.28 Mpc, and ~ 2.43 Mpc respectively. The combined mean maximum distance comes out to be ~ 6.74 Mpc.

We also observe that the maximum distance for all the binaries is observed around the dominant frequency right around the LISA's most sensitive region, e.g., 10 mHz. For BHBH, the maximum distance is observed at 8.498 mHz. The NSNS, BHNS, and NSBH pairs show the maximum distance value at the same frequency, 12.05 mHz. However, when taking the mean for all four DCO types, the dominant frequency corresponding to the maximum distance changes back to 8.498 mHz showing the effects of the most dominantly detected DCO type, BHBH.

V. COMPARATIVE ANALYSIS

In this section, we will deal with the comparative study of our two data sets, Θ_1 and Θ_2 . In order to fairly compare the two, given only the difference of eccentricity, we make use of the seed numbers provided in Θ_1 data set. With the exception of SN kick parameters and eccentricity, all the other parameters were kept the same as in the original data set. We evolved the binaries for Θ_2 consistent with the method described in this paper.

A. Hubble Merger Rate

After running the simulations, we obtained 9751 DCO pairs ($\sim 0.09751\%$). Out of these, only 5178 ($\sim 53.1022\%$) were able to merge within Hubble time, (see table IV).

From table IV RowI we observe that the highest merging rate comes from BHBH as well ($\sim 66.32\%$), followed by BHNS pairs ($\sim 65.87\%$), NSBH ($\sim 63.03\%$) and lastly, NSNS dco type ($\sim 51.57\%$).

Table IV RowII shows that we have NSBH as the dominant detectable DCO type ($\sim 77.93\%$) detections instead of BHBH as in Θ_1 data set. This is followed by BHBH pairs ($\sim 77.25\%$), BHNS pairs ($\sim 68.91\%$) and lastly, NSNS pairs ($\sim 17.46\%$).

| Type | BHBH | NSNS | BHNS | |
|-------|-----------|-------------|-----------|-----------|
| | | | NSBH | BHNS |
| M / T | 189 / 285 | 4438 / 8605 | 358 / 568 | 193 / 293 |
| D / M | 146 / 189 | 775 / 4438 | 279 / 358 | 133 / 193 |

TABLE IV: RowI shows the merging (M) vs total (T) formed DCOs in this study, RowII shows the uniquely detectable (D) vs the merging (M) DCOs from this study for Θ_2 .

The only particular DCO type with a noticeable effect of ZAMS eccentricity is the NSNS type which shows a lot of detections given that the binaries start with eccentric orbits.

B. Detection rates

The Θ_2 data set shows an overall slight increase in the detection rate, (86 – 131) detections against (83 – 124) detection for Θ_1 data set. Although minor overall, the detection rate is significant for BHNS, and NSBH pairs going from (6 – 28) and (13 – 39) in Θ_1 to (11 – 29) and (21 – 46) respectively for Θ_2 over a four year LISA mission.

Similar to appendix C for Θ_1 , appendix D shows the distribution of parameters and average number of DCO detections across the ensemble of the galaxies in this study for Θ_2 . The difference in average number of BHNS detections in the two data set is ~ 18 , the largest, jumping from 33 to 51 for Θ_1 and Θ_2 respectively. Similarly, the NSBH binaries show an average increase of 3 detections. As for BHBH and NSNS pairs, there are more detections in Θ_1 compared to Θ_2 .

It is also noted that the mean parameter values for Θ_2 are also higher than Θ_1 for BHNS, and NSBH pairs, but this might be because of the increased number of detections and vice versa for BHBH, and NSNS pairs.

C. Maximum detection distance

Figure 7 shows the ratio of maximum detection distance between Θ_2 and Θ_1 . We note that the ratio is less than 1 at lower orbital frequencies, from 1×10^{-5} Hz to 1.15×10^{-4} Hz after which increases and only comes below 1 around 1.232×10^{-1} Hz to 1.384×10^{-1} Hz. This suggests that the binaries with circular ZAMS orbits will evolve such that they can be detected to larger distances compared to one with eccentric ZAMS orbits in LISA sensitive band.

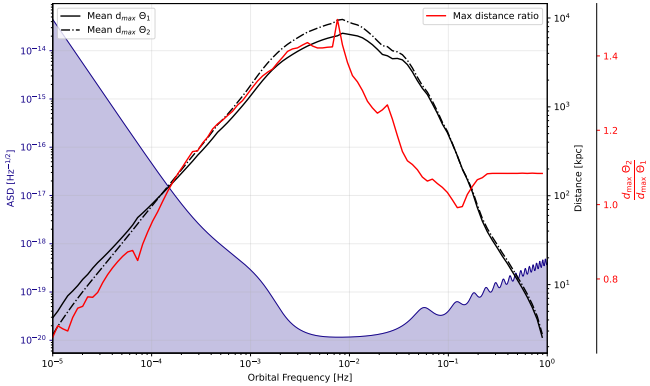


Fig. 7: Mean maximum distance of the two data sets, black solid and dashed lines, and their ratio, red solid line.

D. Final evolutionary stages

A total of 137 seeds were found common between the two data sets. Out of these 140 seeds, 104 were found to evolve to the same final stage before merging in both data sets. The binaries with common and diverging final evolutionary stages are shown in figure 8. The lesser number of diverging cases indicate that the ZAMS eccentricity might not play as much of a bigger role in the development of binary's final stages.

For a better understanding of what the plot is showing, consider the two points highlighted. The red marker on the tail of the arrow shows the DCO stage for the binary in Θ_1 data set, the arrow indicates direction of divergence in evolution with the arrow head showing the final DCO stage of the same binary in Θ_2 data set. On the other hand, the cyan marker indicates no divergence in the evolution, meaning that the binary had the same final evolution stage in both the data sets. The particular binaries in question have seed numbers, 44735 and 1367057 respectively.

E. Two interesting NSNS binaries

Appendix D figure 26 shows a spike in the NSNS SNR plot. This is due to an extremely high value of SNR found in the simulated galaxy number 43, with an average $\log_{10}(\text{SNR})$ of 1.6864 ± 2.7482 . The maximum SNR in that galaxy is of the binary at seed number 6308709. The particulars of this binary are given in table V. The values in the table are rounded off for display purposes.

| $m_{1\text{DCO}}$ | $m_{2\text{DCO}}$ | m_{chirp} | a_{DCO} |
|-------------------------|-------------------|--------------------|-----------------------|
| $1.26 M_\odot$ | $1.91 M_\odot$ | $1.35 M_\odot$ | 0.044 AU |
| e_{DCO} | Z | t_{evol} | t_{lookback} |
| 0.9999 | 0.02595 | 30.135 Myr | 4.967 Myr |
| SNR | MAX SNR harmonics | Galaxy | ϕ |
| 6.8467×10^{14} | 2 | 43 | 6308709 |

TABLE V: Parameters of the NSNS pair with highest SNR in galaxy number 43.

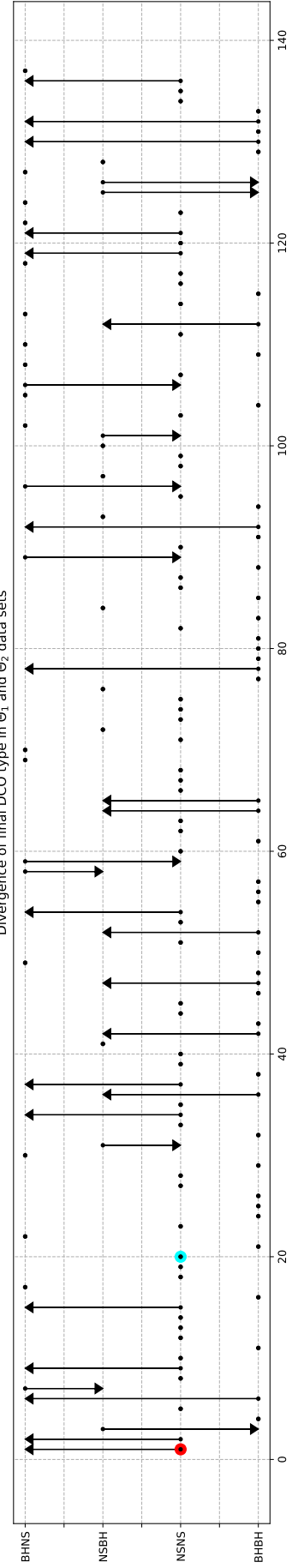


Fig. 8: Plot showing the change in DCO ending states for the common seed numbers from Θ_1 and Θ_2 data sets. The direction of arrows shows the change in the DCO type from Θ_1 and Θ_2 data set. The binaries that didn't change the DCO type after evolution are represented by a filled dot.

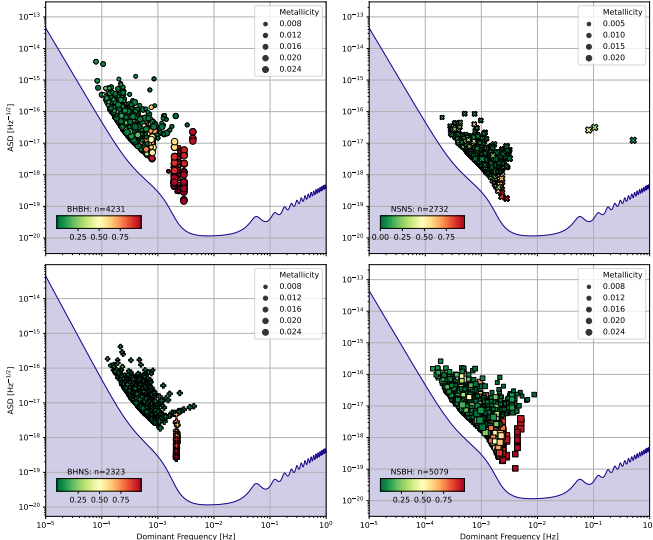


Fig. 9: Same as figure 2 but for Θ_2 data set.

Upon further investigations, we came to know that the binary might have merged already. The LISA parameters, e_{LISA} , a_{LISA} , f_{LISA} , for said binary show that the semi-major axis and eccentricity for this binary at the time of SNR detection are 8.66×10^{-51} AU and 10.34×10^{-72} respectively. The extremely high SNR also accompanies an equally high dominant frequency, out of the plotting range, of roughly 1.4×10^{68} Hz and an undefined ASD value. We show the detections of Θ_2 is figure 9. The binary discussed above, with seed number 6308709, is not visible in this plot.

There are three more NSNS pairs that are out of characteristics, and all three are the same pair with seed number 1699345.

| LISA parameters for $\phi = 1699345$ | | | | |
|--------------------------------------|---------------------------------------|--|--|-------------------|
| | $f_{\text{orb}} \times 10^{-3}$ Hz | $f_{\text{dom}} \times 10^{-17}$ Hz $^{-1/2}$ | $a_{\text{LISA}} \times 10^{-3}$ R $_{\odot}$ | e_{LISA} |
| 1 | 27.318 | 2.611 | 35.384 | 0.4175 |
| 2 | 52.504 | 3.155 | 22.890 | 0.2601 |
| 3 | 255.01 | 1.236 | 7.981 | 0.0554 |

TABLE VI: LISA parameters for binary with $\phi = 1699345$ obtained by LEGWORK before SNR calculations.

REFERENCES

- [1] Abbott, B. P., Abbott, R., Abbott, T. D., et al. 2017, ApJ, 848, L13, doi: [10.3847/2041-8213/aa920c](https://doi.org/10.3847/2041-8213/aa920c)
- [2] Acernese, F. a., Agathos, M., Agatsuma, K., et al. 2014, Classical and Quantum Gravity, 32, 024001
- [3] Andrews, J. J., Breivik, K., Pankow, C., D’Orazio, D. J., & Safarzadeh, M. 2020, ApJ, 892, L9, doi: [10.3847/2041-8213/ab5b9a](https://doi.org/10.3847/2041-8213/ab5b9a)
- [4] Babak, S., Baker, J. G., Benacquista, M. J., et al. 2008, Classical and Quantum Gravity, 25, 114037
- [5] —. 2010, Classical and Quantum Gravity, 27, 084009
- [6] Barack, L., & Cutler, C. 2004, Phys. Rev. D, 69, 082005, doi: [10.1103/PhysRevD.69.082005](https://doi.org/10.1103/PhysRevD.69.082005)
- [7] Barrett, J. W., Gaebel, S. M., Neijssel, C. J., et al. 2018, MNRAS, 477, 4685
- [8] Belczynski, K., Benacquista, M., & Bulik, T. 2010, ApJ, 725, 816, doi: [10.1088/0004-637X/725/1/816](https://doi.org/10.1088/0004-637X/725/1/816)
- [9] Błaut, A., Babak, S., & Królak, A. 2010, Phys. Rev. D, 81, 063008
- [10] Bovy, J., Leung, H. W., Hunt, J. A. S., et al. 2019, MNRAS, 490, 4740, doi: [10.1093/mnras/stz2891](https://doi.org/10.1093/mnras/stz2891)
- [11] Bovy, J., Rix, H.-W., Schlafly, E. F., et al. 2016, ApJ, 823, 30, doi: [10.3847/0004-637X/823/1/30](https://doi.org/10.3847/0004-637X/823/1/30)
- [12] Broekgaarden, F. S., Justham, S., de Mink, S. E., et al. 2019, MNRAS, 490, 5228
- [13] Broekgaarden, F. S., Berger, E., Neijssel, C. J., et al. 2021, MNRAS, 508, 5028, doi: [10.1093/mnras/stab2716](https://doi.org/10.1093/mnras/stab2716)
- [14] Chapman-Bird, C. E. A., Berry, C. P. L., & Woan, G. 2022, arXiv e-prints, arXiv:2212.06166
- [15] Collaboration, L. S., & Aasi, J. 2015, Class. Quantum Gravity, 32, 074001
- [16] Digman, M. C., & Hirata, C. M. 2022, arXiv e-prints, arXiv:2212.14887
- [17] Eddington, A. S. 1922, Proceedings of the Royal Society of London Series A, 102, 268
- [18] Einstein, A. 1916, Sitzungsberichte der Königlich Preußischen Akademie der Wissenschaften (Berlin), 688
- [19] Finn, L. S., & Thorne, K. S. 2000, Phys. Rev. D, 62, 124021, doi: [10.1103/PhysRevD.62.124021](https://doi.org/10.1103/PhysRevD.62.124021)
- [20] Frankel, N., Rix, H.-W., Ting, Y.-S., Ness, M., & Hogg, D. W. 2018, ApJ, 865, 96, doi: [10.3847/1538-4357/aadba5](https://doi.org/10.3847/1538-4357/aadba5)
- [21] Fryer, C. L., Belczynski, K., Wiktorowicz, G., et al. 2012, ApJ, 749, 91
- [22] Fumagalli, J., Pieroni, M., Renaux-Petel, S., & Witkowski, L. T. 2022, JCAP, 2022, 020, doi: [10.1088/1475-7516/2022/07/020](https://doi.org/10.1088/1475-7516/2022/07/020)
- [23] Gair, J. R., Babak, S., Sesana, A., et al. 2017, in Journal of Physics Conference Series, Vol. 840, Journal of Physics Conference Series, 012021
- [24] Guo, H.-K., Shu, J., & Zhao, Y. 2017, arXiv e-prints, arXiv:1709.03500
- [25] Hulse, R. A., & Taylor, J. H. 1975, ApJ, 195, L51
- [26] Hurley, J. R., Pols, O. R., & Tout, C. A. 2000, MNRAS, 315, 543
- [27] Hurley, J. R., Tout, C. A., & Pols, O. R. 2002, MNRAS, 329, 897
- [28] Khakhaleva-Li, Z., & Hogan, C. J. 2020, arXiv, arXiv:2006.00438, arXiv: [2006.00438](https://arxiv.org/abs/2006.00438)
- [29] Klein, A., Barausse, E., Sesana, A., et al. 2016, Phys. Rev. D, 93, 024003
- [30] Korol, V., Rossi, E. M., & Groot, P. J. 2017, in Astronomical Society of the Pacific Conference Series, Vol. 509, 20th European White Dwarf Workshop, ed. P. E. Tremblay, B. Gaensicke, & T. Marsh, 529
- [31] Kroupa, P. 2001, MNRAS, 322, 231, doi: [10.1046/j.1365-8711.2001.04022.x](https://doi.org/10.1046/j.1365-8711.2001.04022.x)
- [32] Lau, M. Y. M., Mandel, I., Vigna-Gómez, A., et al. 2020, MNRAS, 492, 3061, doi: [10.1093/mnras/staa002](https://doi.org/10.1093/mnras/staa002)
- [33] Mandel, I., & Müller, B. 2020, MNRAS, 499, 3214
- [34] McMillan, P. J. 2011, MNRAS, 414, 2446, doi: [10.1111/j.1365-2966.2011.18564.x](https://doi.org/10.1111/j.1365-2966.2011.18564.x)
- [35] Nelemans, G., Yungelson, L. R., & Portegies Zwart, S. F. 2001, A&A, 375, 890
- [36] Öpik, E. 1924, Publications of the Tartu Astrofizica Observatory, 25, 1
- [37] Peters, P. C. 1964, Physical Review, 136, 1224, doi: [10.1103/PhysRev.136.B1224](https://doi.org/10.1103/PhysRev.136.B1224)
- [38] Peters, P. C., & Mathews, J. 1963, Physical Review, 131, 435, doi: [10.1103/PhysRev.131.435](https://doi.org/10.1103/PhysRev.131.435)
- [39] Prince, T. A., Tinto, M., Larson, S. L., & Armstrong, J. W. 2002, Phys. Rev. D, 66, 122002, doi: [10.1103/PhysRevD.66.122002](https://doi.org/10.1103/PhysRevD.66.122002)
- [40] Renzo, M., Callister, T., Chatzioannou, K., et al. 2021, ApJ, 919, 128, doi: [10.3847/1538-4357/ac1110](https://doi.org/10.3847/1538-4357/ac1110)
- [41] Riley, J., Mandel, I., Marchant, P., et al. 2021, MNRAS, 505, 663
- [42] Riley, J., Agrawal, P., Barrett, J. W., et al. 2022, ApJS, 258, 34, doi: [10.3847/1538-4365/ac416c](https://doi.org/10.3847/1538-4365/ac416c)
- [43] Robson, T., Cornish, N. J., & Liu, C. 2019, Classical and Quantum Gravity, 36, 105011, doi: [10.1088/1361-6382/ab1101](https://doi.org/10.1088/1361-6382/ab1101)
- [44] Ruiter, A. J., Belczynski, K., Benacquista, M., Larson, S. L., & Williams, G. 2010, ApJ, 717, 1006
- [45] Sana, H., de Mink, S. E., de Koter, A., et al. 2012, Science, 337, 444, doi: [10.1126/science.1223344](https://doi.org/10.1126/science.1223344)
- [46] Sesana, A., Volonteri, M., & Haardt, F. 2009, Classical and Quantum Gravity, 26, 094033, doi: [10.1088/0264-9381/26/9/094033](https://doi.org/10.1088/0264-9381/26/9/094033)
- [47] Shao, Y., & Li, X.-D. 2021, ApJ, 920, 81, doi: [10.3847/1538-4357/ac173e](https://doi.org/10.3847/1538-4357/ac173e)
- [48] Stevenson, S., Vigna-Gómez, A., Mandel, I., et al. 2017, Nat. Commun., 8, 14906, doi: [10.1038/ncomms14906](https://doi.org/10.1038/ncomms14906)
- [49] Taylor, J. H., & Weisberg, J. M. 1982, ApJ, 253, 908
- [50] Vigna-Gómez, A., Neijssel, C. J., Stevenson, S., et al. 2018, MNRAS, 481, 4009
- [51] Wagg, T., Breivik, K., & de Mink, S. E. 2022, ApJS, 260, 52, doi: [10.3847/1538-4365/ac5c52](https://doi.org/10.3847/1538-4365/ac5c52)
- [52] Wagg, T., Broekgaarden, F. S., de Mink, S. E., et al. 2021, arXiv e-prints, arXiv:2111.13704, arXiv: [2111.13704](https://arxiv.org/abs/2111.13704)
- [53] Wegg, C., Gerhard, O., & Portail, M. 2015, MNRAS, 450, 4050
- [54] Willems, B., Kalogera, V., Vecchio, A., et al. 2007, ApJ, 665, L59
- [55] Yu, S., & Jeffery, C. S. 2010, A&A, 521, A85

APPENDIX A SETTINGS FOR USING COMPAS

To generate a binary systems, COMPAS requires the following parameters from the user as discussed earlier,

- mass of primary star ($m_{1\text{ZAMS}}$),
- mass of secondary star ($m_{2\text{ZAMS}}$),
- semi-major axis of the orbit (a_{ZAMS}),
- random seed (ϕ)
- remnant mass prescription,
- eccentricity of the orbit (e_{ZAMS}), and
- metallicity of the stars (Z).

We've discussed the first four parameters in the main text, here we will discuss the selection of eccentricity and metallicity values.

ECCENTRICITY

In order to evaluate whether the initial eccentricity affects GW emission at the end stages of the DCO, we generate two identical data sets. For the primary data set, we chose the eccentricity value to be varied between 0 and 1.

However, we noticed that some stars within the population synthesis had a ZAMS stellar type of 16. This refers to chemically homogeneously evolving stars [41, 42]. These binaries were found to have zero eccentricity even when the parameter was chosen to be within the range (0, 1).

For the other data set we take the eccentricity value to be 0 for all the generated binaries.

METALLICITY

One of the major challenges in generation of the stellar binaries for this study was the selection of a distribution which will result in stars at the higher end of COMPAS metallicity boundary, $z = 0.03$. A power-law, gamma, and beta distributions were selected to try and simulate the required metallicity distribution. In the following section, we discuss the selected distributions briefly,

A. Power law distribution

The random values for metallicity were generated using the power law distribution given below,

$$f(x, a) = ax^{(a-1)} \quad (7)$$

where a is the index of the power law distribution.¹⁰ Figure 10 shows the plot for the probability density function (PDF) of the power law with $a \in [1, 2]$. Although the distribution can produce higher values, it does not suppress the lower values so this distribution was discarded.

¹⁰<https://docs.scipy.org/doc/scipy/reference/generated/scipy.stats.powerlaw.html>

B. Gamma distribution

For the probability density function for gamma distribution,¹¹ we use the following form,

$$f(x, a) = \frac{x^{a-1} \exp(-x)}{\Gamma(a)} \quad (8)$$

for $x \geq 0$ and $a > 0$. Here, a is the shape factor, and Γ is the gamma function, such that $\Gamma(a) = (a - 1)!$. Similar to the power law distribution, the gamma distribution (see, figure 11) was not a good selection for the values of metallicity that were required for this study.

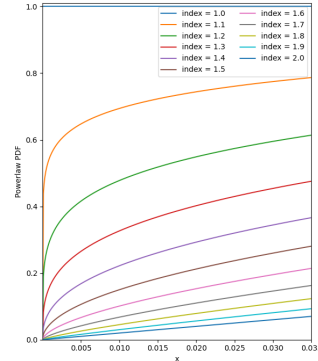


Fig. 10: PL distribution

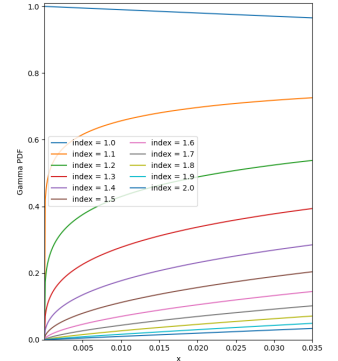


Fig. 11: Γ distribution

C. Beta distribution

For the beta distribution, we use the following form,

$$f(x, a, b) = \frac{\Gamma(a+b)x^{a-1}(1-x)^{b-1}}{\Gamma(a)\Gamma(b)} \quad (9)$$

For $0 \leq x \leq 1$, $a > 0$, $b > 0$ and Γ is the gamma function.¹²

Figure 12 shows the beta distribution with a fixed $\beta = 80$. Similarly, figure 13 shows the beta distribution with a fixed $\alpha = 5$. For our case, we selected Beta(5, 80) as our distribution of choice for metallicity and generated 10^7 values between the COMPAS limits $10^{-4} < z < 0.03$.

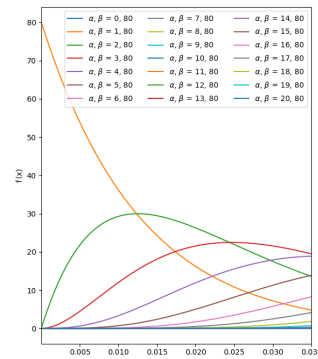


Fig. 12: Beta distribution with varying α and fixed β parameter.

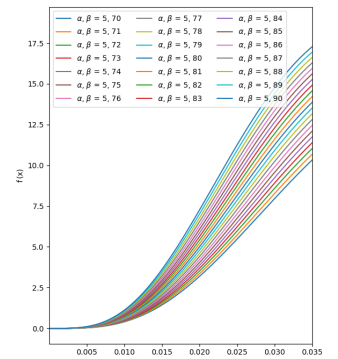


Fig. 13: Beta distribution with fixed α and varying β parameter.

¹¹<https://docs.scipy.org/doc/scipy/reference/generated/scipy.stats.gamma.html>

¹²<https://docs.scipy.org/doc/scipy/reference/generated/scipy.stats.beta.html>

APPENDIX B THE MILKY WAY MODEL

In this section, we will briefly outline the milky way galaxy model used in this study. The model is developed by [52] and makes use of the galaxy's enrichment history by taking into account the metallicity-radius-time relationship [20]. It uses a separate star formation history and spatial distribution for the low-[α/Fe], high-[α/Fe] discs, and bulge in the galaxy.

A. Star formation rate

The star formation rate for both the low-[α/Fe] and high-[α/Fe] disks is expressed as,

$$p(\tau) \propto \exp\left(-\frac{\tau_m - \tau}{\tau_{\text{SFR}}}\right), \quad (10)$$

where τ is the time difference between the star's ZAMS stage and today. The age of milky way galaxy, τ_m , is taken as 12 Gyr, and the star formation rate as, $\tau_{\text{SFR}} = 6.8$ Gyr. The star-forming period of low-[α/Fe] and high-[α/Fe] discs were taken as 0 Gyr to 8 Gyr and 8 Gyr to 12 Gyr respectively. The model adopts 6 Gyr to 12 Gyr as the star-forming period of the bulge [10].

B. Radial distribution

The radial distribution of stars within the milky way galaxy was performed using the following expression,

$$p(R) = \exp\left(-\frac{R}{R_d}\right) \frac{R}{R_d^2} \quad (11)$$

However, a different scale length, R_d , was chosen for each component of the galaxy. For low-[α/Fe], the model uses $R_{\text{exp}}(\tau)$ as the scale length [20, Eq 6], where

$$R_{\text{exp}}(\tau) = 4 \text{ kpc} \left[1 - \alpha_{R_{\text{exp}}} \left(\frac{\tau}{8 \text{ Gyr}} \right) \right], \quad (12)$$

with the value of inside-out growth parameter, $\alpha_{R_{\text{exp}}}$, as 0.3. For high-[α/Fe] disc and bulge, the value of scale length was chosen as (1/0.43) kpc and 1.5 kpc respectively.

C. Vertical distribution

The model employs a similar method of single exponent expression with varying scale height parameters for the vertical distribution as well. The exponential expression used is,

$$p(|z|) = \frac{1}{z_d} \exp\left(-\frac{|z|}{z_d}\right), \quad (13)$$

where z here is the vertical displacement from the galactic plane. The scale height parameter, z_d , for low-[α/Fe], high-[α/Fe] and bulge was taken as 0.3 kpc [34], 0.95 kpc [11], and 0.2 kpc [53] respectively.

D. Metallicity-radius-time relationship

The MRT relationship plays an important part, both in the galaxy model and later on in the placement of DCOs within the galaxy as well. The model makes use of [20, Eq. 7],

$$\begin{aligned} [\text{Fe}/\text{H}](R, \tau) &= F_m + \nabla[\text{Fe}/\text{H}]R \\ &- \left(F_m + \nabla[\text{Fe}/\text{H}]R_{[\text{Fe}/\text{H}] = 0}^{\text{now}} \right) f(\tau) \end{aligned} \quad (14)$$

For each point generated, if the value of metallicity produced by the MW model was less or greater than the limits defined by COMPAS¹³ it was changed to a uniformly drawn random number between $\text{COMPAS}_{\min} - \text{ZSOLAR}$ and $\text{ZSOLAR} - \text{COMPAS}_{\max}$ respectively.

E. Galaxy synthesis

For the synthesis of an instance of the Milky Way galaxy, the model described previously samples the following parameters,

$$\theta_i = \{\tau, D, z, \text{component}\},$$

where τ is the look-back time for the binary, D is the distance from Earth, z is the metallicity, and 'component' is the component of the galaxy in which the binary resides.¹⁴ The parameters are generated for $i = 1, 2, 3, \dots, N_{\text{GAL}}$, where $N_{\text{GAL}} = 100$.

¹³0.0001, 0.03

¹⁴One of the three, low-[α/Fe] disc, high-[α/Fe] disc, or bulge.

APPENDIX C

PARAMETER DISTRIBUTION ACROSS THE GALAXIES – Θ_1

A. Binary Black Holes

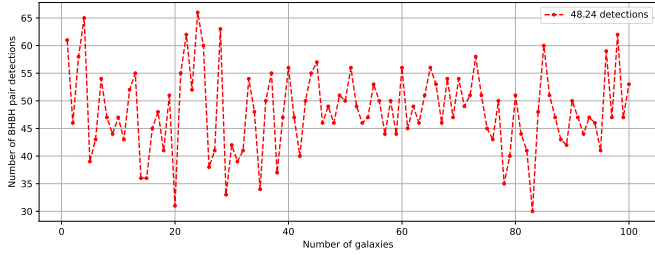


Fig. 14: Number of BHBH pair detection per galaxy instance. On average, a total of ~ 48 pairs per galaxy were detected in this study.

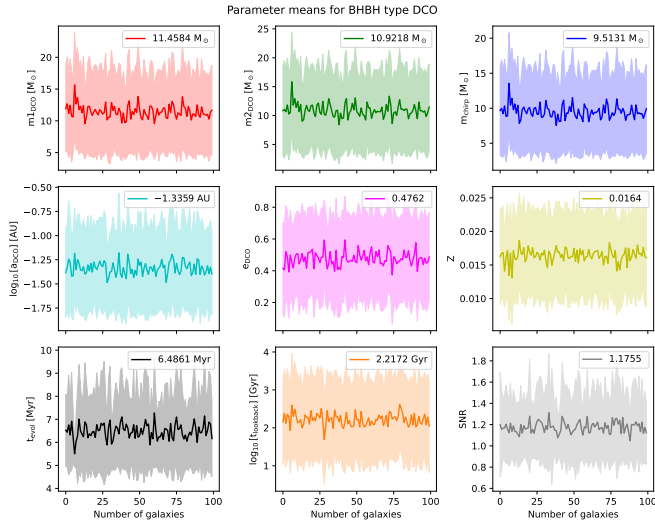


Fig. 15: The mean and standard deviation for selected parameters in every galaxy, plotted against the galaxy number. An overall measure of mean and standard deviation of all the galaxies is also shown for the selected parameters.

B. Binary Neutron Stars

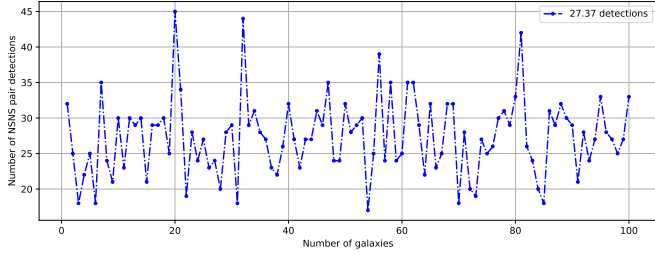


Fig. 16: Number of NSNS pair detection per galaxy instance. On average, a total of ~ 27 pairs per galaxy were detected in this study.

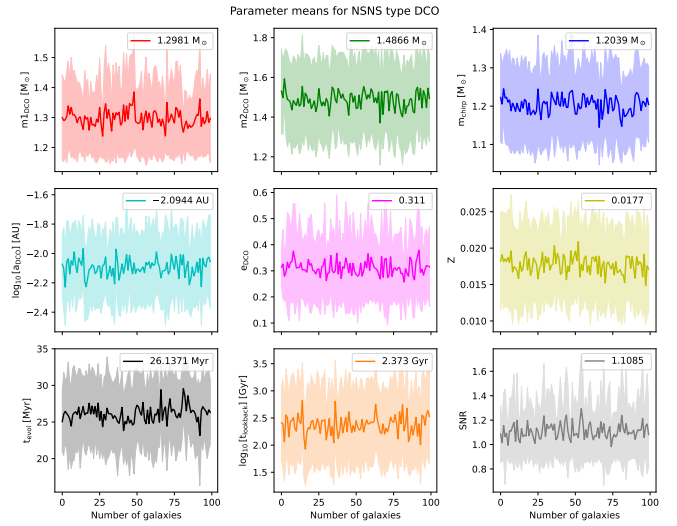


Fig. 17: Same as figure 15.

C. Neutron Star – Black Hole binary

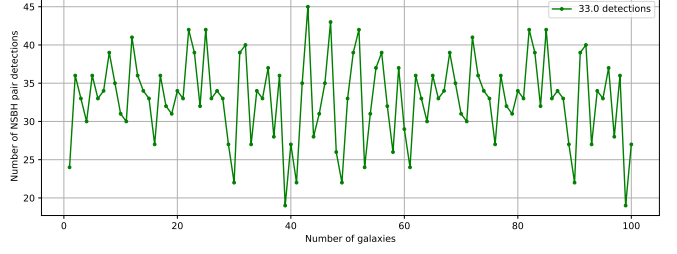


Fig. 18: Number of NSBH pair detection per galaxy instance. On average, a total of ~ 33 pairs per galaxy were detected in this study.

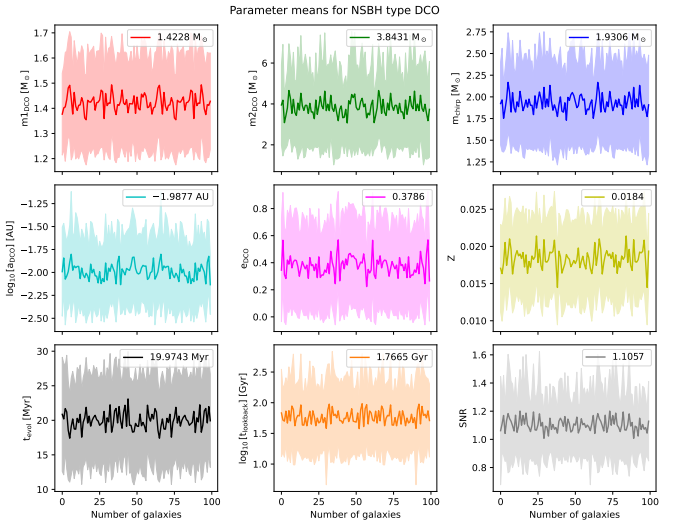


Fig. 19: Same as figure 15.

D. Black Hole – Neutron Star binary

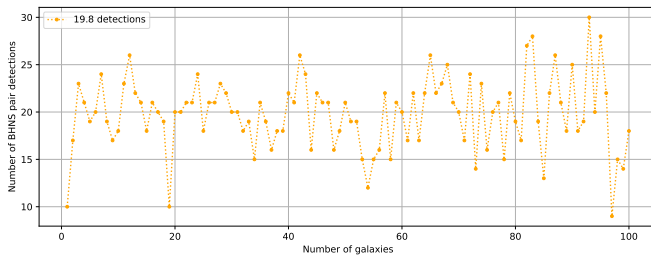


Fig. 20: Number of BHNS pair detection per galaxy instance. On average, a total of ~ 20 pairs per galaxy were detected in this study.

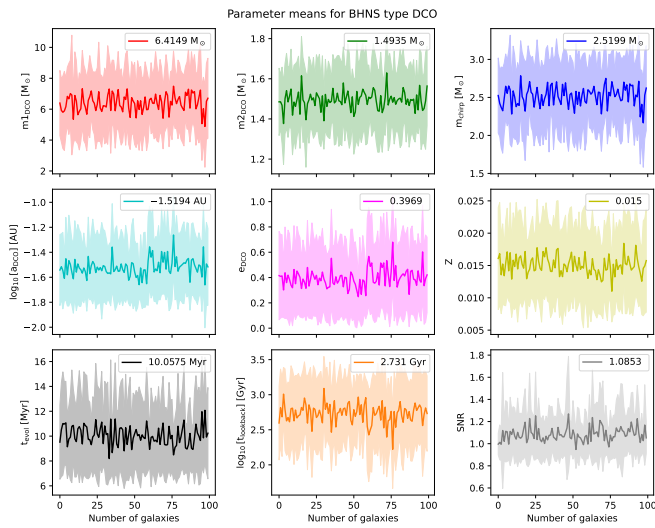


Fig. 21: Same as figure 15.

APPENDIX D PARAMETER DISTRIBUTION ACROSS THE GALAXIES – Θ_2

A. Binary Black Holes

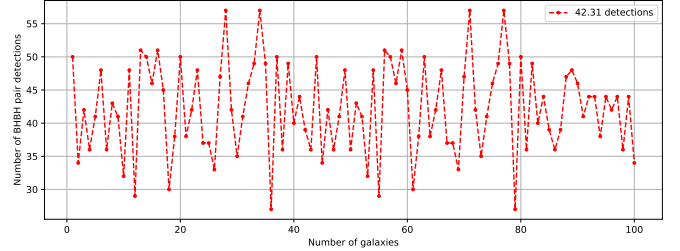


Fig. 22: Number of BHBH pair detection per galaxy instance. On average, a total of ~ 42 pairs per galaxy were detected in this study.

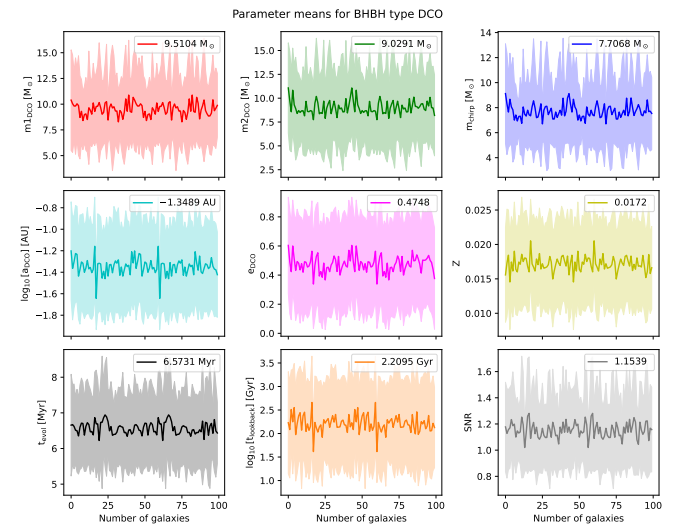


Fig. 23: The mean and standard deviation for selected parameters in every galaxy, plotted against the galaxy number. An overall measure of mean and standard deviation of all the galaxies is also shown for the selected parameters.

B. Binary Neutron Stars

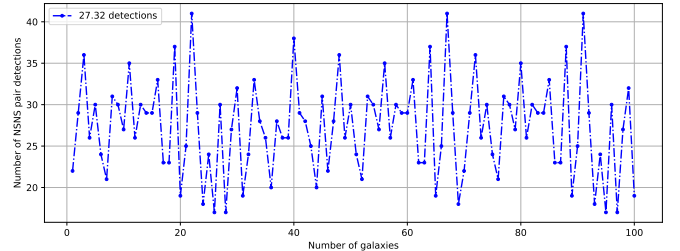


Fig. 24: Number of NSNS pair detection per galaxy instance. On average, a total of ~ 27 pairs per galaxy were detected in this study.

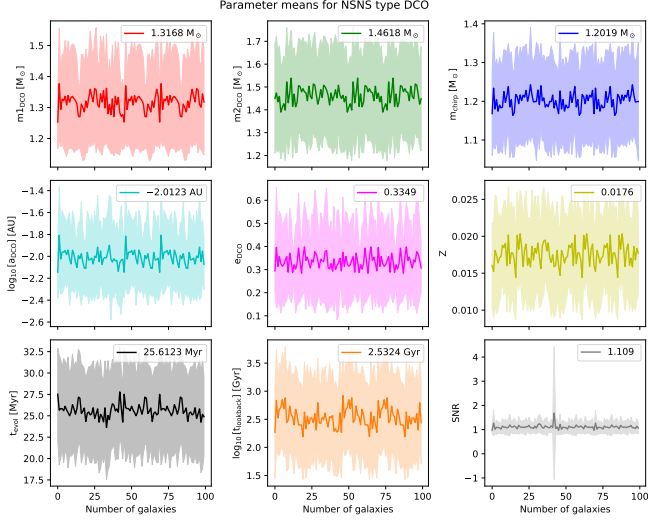


Fig. 25: Same as figure 23.

C. Neutron Star – Black Hole binary

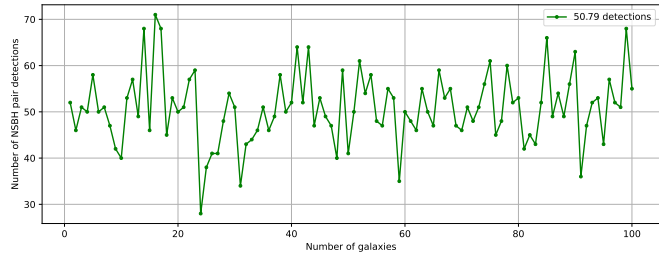
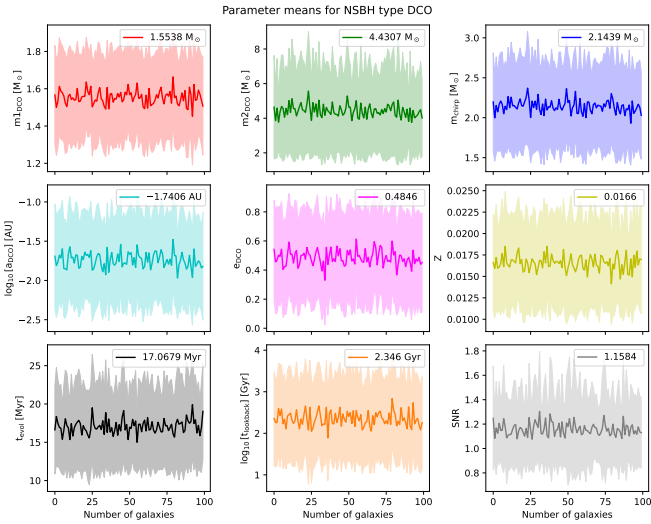
Fig. 26: Number of NSBH pair detection per galaxy instance. On average, a total of ~ 51 pairs per galaxy were detected in this study.

Fig. 27: Same as figure 23.

D. Black Hole – Neutron Star binary

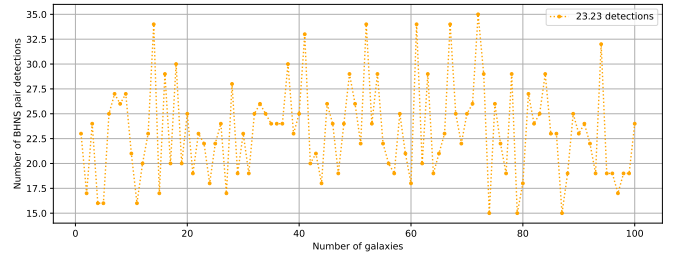
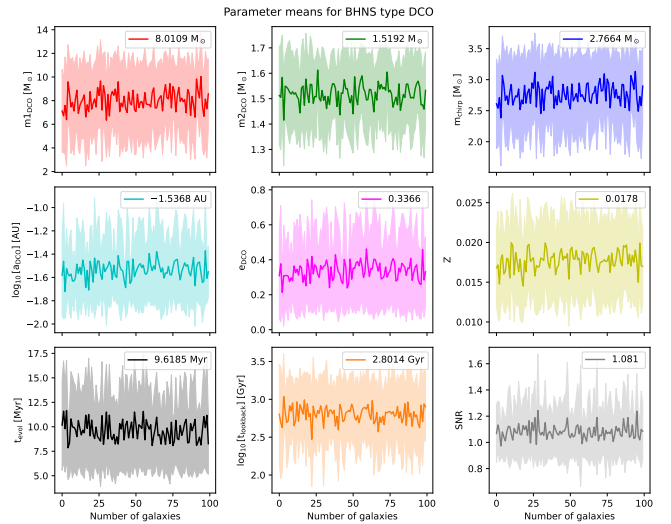
Fig. 28: Number of BHNS pair detection per galaxy instance. On average, a total of ~ 23 pairs per galaxy were detected in this study.

Fig. 29: Same as figure 23.